Measurement 287 (2026) 122366

Contents lists available at ScienceDirect

Measurement

journal homepage: www.elsevier.com/locate/measurement

Cross-instrument measurement framework linking X-ray μCT and photoluminescence spectroscopy: Application to microcracks characterization in mineralized enamel

Irma Dumbryte [a,*], Donatas Narbutis [b], Maria Androulidaki [c], Edvinas Skliutas [d], Robertas Virketis [e], Elena Jasiuniene [f,g], Saulius Juodkazis [h,i], Greta Merkininkaite [e], Mangirdas Malinauskas [d]

[a] Institute of Dentistry, Faculty of Medicine, Vilnius University, Zalgirio str. 117, LT-08217 Vilnius, Lithuania
[b] Institute of Theoretical Physics and Astronomy, Faculty of Physics, Vilnius University, Sauletekio Ave. 9, LT-10222 Vilnius, Lithuania
[c] Microelectronics Research Group, Institute of Electronic Structure & Laser, Foundation for Research and Technology FORTH-Hellas, P.O. BOX 1527, Vassilika Vouton, Heraklion 711 10, Crete, Hellas, Greece
[d] Laser Research Center, Faculty of Physics, Vilnius University, Sauletekio Ave. 10, LT-10223 Vilnius, Lithuania
[e] Institute of Chemistry, Faculty of Chemistry and Geosciences, Vilnius University, Naugarduko str. 24, LT-03225 Vilnius, Lithuania
[f] Ultrasound Research Institute, Kaunas University of Technology, Barsausko str. 59-A423, LT-51423 Kaunas, Lithuania
[g] Department of Electronics Engineering, Kaunas University of Technology, Studentu str. 50, LT-51368 Kaunas, Lithuania
[h] Optical Sciences Centre and ARC Training Centre in Surface Engineering for Advanced Materials (SEAM), School of Science, Swinburne University of Technology, Hawthorn, VIC 3122, Australia
[i] WRH Program International Research Frontiers Initiative (IRFI) Tokyo Institute of Technology, Nagatsuta-cho, Midori-ku, Yokohama 226-8503, Japan

ARTICLE INFO

Keywords:
Correlative imaging
Defect characterization
Elemental mapping
Multimodal analysis
Spectro-spatial registration

ABSTRACT

Correlative characterization of micro-scale defects in heterogeneous mineralized materials requires the spatial fusion of measurement modalities that differ in resolution, contrast mechanism, and coordinate system. This study presents a non-destructive multimodal measurement methodology in which X-ray micro-computed tomography (μCT) and spatially selective photoluminescence (PL) spectroscopy are linked on an intact specimen by a 3D surface mesh-assisted spatial registration framework, with complementary energy-dispersive X-ray spectroscopy (EDS) used to characterize the associated compositional changes. The registration aligns the volumetric and point-resolved measurements with a spatial uncertainty bounded by the PL laser spot size (diameter $\approx$ 80 μm) and the μCT voxel size ($\approx 7 \times 7 \times 7$ μm^3), both smaller than the spacing between adjacent measurement points, ensuring well-defined co-localization of crack-affected and pristine regions. The methodology was demonstrated on extracted human premolars with visible enamel microcracks: 192 polarization-resolved PL spectra per tooth, acquired at 325 nm excitation across 12 spatial positions (6 cracked, 6 pristine) and spatially registered to the μCT datacube, revealed a reproducible difference in spectral shape between crack-affected and pristine regions. A peak asymmetry index, defined as the ratio of the two emission maxima, was reduced in cracked regions consistently in both teeth and significantly when pooled across specimens (1.16 *vs* 1.28; p = 0.014), supported by EDS evidence of increased carbon content at crack sites (a 42% relative increase in averaged carbon content, with the carbon-to-oxygen ratio rising from 0.46 to 0.84). The validated measurement framework — its spatial registration with bounded uncertainty — is material-independent and generalizable to correlative volumetric and spectroscopic defect characterization in heterogeneous solids.

* Corresponding author.
E-mail address: irma.dumbryte@mf.vu.lt (I. Dumbryte).

https://doi.org/10.1016/j.measurement.2026.122366
Received 3 March 2026; Received in revised form 23 June 2026; Accepted 25 June 2026
Available online 2 July 2026

1. Introduction

Non-destructive characterization of microcracks (MCs) in heterogeneous mineralized materials is challenging due to differences in the spatial resolution and contrast mechanisms between imaging methods. No single modality simultaneously provides high spatial resolution, volumetric coverage, chemical specificity, and structural sensitivity; therefore, comprehensive characterization requires correlative measurement — the spatial fusion of data acquired by instruments whose imaging principles, length scales, and coordinate systems differ. The metrological difficulty arises not from individual techniques, but from their integration: the validated superimposition of one method onto another, the clear handling of uncertainties associated with the fused data, and the repeatability and reproducibility of the combined measurement chain. Although these requirements are well established in metrology, they are only partially addressed for hard mineralized tissues, particularly tooth enamel.

Tooth enamel serves as an excellent example here, being hierarchically structured, anisotropic, and heterogeneous at the very scale at which correlative measurement is needed. It is the most highly mineralized tissue of the human body and consists of 95 wt% mineral (in mature enamel), 1 wt% soft organic matrix, and 4 wt% water [1]. On the microstructural level the inorganic part is composed of crystal rods (sometimes called prisms) and each single enamel rod is comprised of bundles of nanometer-scale carbonated hydroxyapatite (HAP) crystals ($\approx 25\,\text{nm}$ thick, $\approx 100\,\text{nm}$ wide, and $\geq 100\,\text{nm}$ long) [2–4]. Every rod is surrounded by a sheath of organic matrix [5], and the intra-rod crystals are being separated by nanochannels or pores that may extend for long distances through the enamel rods and only terminate at a rod boundary or free surface [6–8]. The arrangement of the rods depends on their location: in the enamel closest to the tooth surface, the rods extend in a nearly parallel manner, while in the enamel close to the dentin-enamel junction (DEJ), the rods extend within groups that are obliquely oriented to one another [2,4]. This microstructure of the enamel and the arrangement of its mineral and organic components determine enamel-specific mechanical properties (i.e., high fracture toughness and resistance to crack growth) [2,4,9–11] and give rise to an anisotropic optical response, which can complicate the interpretation of any single measurement modality.

Within this structure, enamel MCs are a form of tooth damage that can develop due to temperature variations, abnormalities in the maturation process, occlusal forces (e.g., generated during pathological tooth wear), traumatic injuries (e.g., caused by tooth extraction procedure), restorative processes [12–16], and even orthodontic forces exerted during removal of brackets at the end of treatment [12,17–23]. Their reported dimensions - width range of $0.25-35.04\,\mu\text{m}$ [4], length range of $0.24-10.15\,\text{mm}$ [4], and depth up to $\approx 1\,\text{mm}$ [24–26] - encompass the resolution and field of view of several complementary methods, and the cracks themselves are heterogeneous in their geometry and chemical composition, making them an ideal subject for correlative measurements.

Recent applications of X-ray micro-computed tomography (μCT) for cracks analysis have expanded our knowledge of this form of tooth damage [22,27]. X-ray μCT has been validated as a powerful method for 3D qualitative (and potentially quantitative) examination of enamel MCs with distinct precision and versatility [22,27]. Photoluminescence (PL) spectroscopy is one of the complementary analytical methods to characterize the optical properties of the material by measuring its light emission after being excited by a light source, typically a laser or ultraviolet light [28]. The optical characteristics of natural teeth [29,30] and fluorescence variations between sound enamel and enamel affected by caries [31–33], white spot lesions [33], or bleaching treatments [34] at 337.8 nm [31], 395 nm [33], 405 nm [32] excitation have already been studied. Energy-dispersive X-ray spectroscopy (EDS), applied conventionally to sectioned samples, has revealed the elemental changes during the demineralization process [35–37]. A recent example combined fluorescence and reflectance hyperspectral imaging for caries diagnosis; however, such approaches pair two 2D optical modalities and do not address a 3D volumetric-plus-spectroscopic combination on an intact tooth. Until now, however, these modalities have been applied either in isolation or to individual samples and separate regions, which makes it impossible to directly combine the data [38]; no comparable correlative framework has been reported for intact (unsectioned) non-flat tooth tissue with a spatial registration of characterized spatial uncertainty.

Existing methods for characterizing MCs in mineralized solids suffer from three measurement-science limitations. First, conventional EDS and scanning electron microscopy (SEM) mapping require sectioning or polishing the specimen, which destroys the 3D crack network and introduces surface-preparation artifacts. Second, single-technique measurements cannot independently determine whether the material properties within the cracked enamel differ significantly from those of the surrounding pristine (good/sound) areas, and whether these changes lead to a loss of structural integrity at the MC site. Third, the small size of the MC [4,22,24–27] and the resolution of the imaging technique make it difficult to identify the same MC even with the same imaging method. In 3D X-ray data, some cracks are smaller than the voxel size ($\approx 7 \times 7 \times 7\ \mu\text{m}^3$) and have a variable signal-to-noise ratio. An even greater challenge is to find and characterize the same MC across different techniques, for example, to identify the position of the laser spot on the tooth surface during PL measurements. No prior multi-technique study of tooth tissue has reported a cross-instrument spatial registration with characterized spatial uncertainty, which is necessary to measure the same region with each technique rather than comparing similar-looking regions measured separately.

Thus, the aim of this study was to develop and demonstrate a correlative measurement methodology that maps X-ray μCT images with PL of the same crack-affected and pristine enamel regions, linked through a 3D surface mesh–assisted spatial registration framework with bounded spatial uncertainty, and uses complementary EDS to characterize the corresponding compositional changes (Fig. 1(a–e)). The methodology is demonstrated on extracted human premolars with enamel MCs as a representative heterogeneous mineralized material, with a further objective of assessing the structural integrity of the teeth along the crack.

2. Methods

The correlative measurement workflow combined two modalities — X-ray μCT and PL spectroscopy — co-registered on an intact tooth. The microcracks were first identified and selected visually by varying the viewing and light source angles. Subsequently, they were confirmed using SEM images. Photoluminescence measurements were then made on the affected and pristine areas of the chosen cracks by carefully selecting the location of the laser spot. Finally, the positions of PL measurements were overlaid on the X-ray data to confirm whether the cracks had extended in depth. It is important to emphasize that although some cracks are not visible on X-rays, this is due to the limited resolution, and the identification of crack-affected and pristine regions is based on optical examination. The accuracy of the spatial registration linking the modalities is addressed in Section 2.2.2.

2.1. Samples and protocols

Enamel MCs and pristine tooth areas around the crack were studied in this work. After atraumatic tooth extraction using a special instrument by an experienced oral surgeon, two maxillary premolars with visible cracks on the buccal and palatal surfaces of the tooth were prepared following the guidelines of the International Organization for Standardization (ISO/TS 11405; 2015), and kept in a hydrated environment (distilled water) except for short periods during experiments. Written informed consent was obtained from all the participants and/or

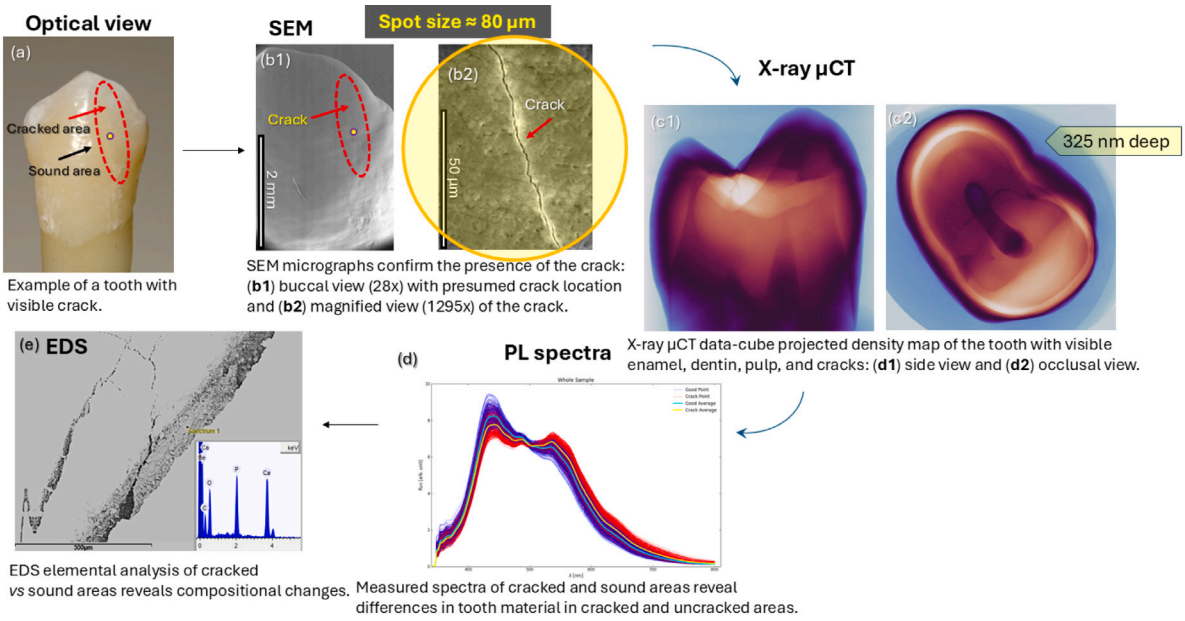

Fig. 1. Overview of the correlative measurement workflow on a tooth with a visible enamel crack: (a) optical view; (b) SEM micrographs at two magnifications; (c) X-ray μCT projected density map (the arrow marks the 325 nm light-penetration depth); (d) PL spectra of cracked and pristine areas; (e) EDS elemental analysis.

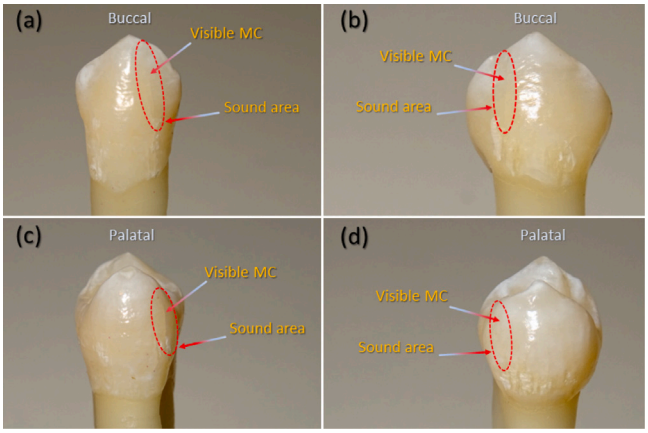

Fig. 2. Photographs of two teeth with visible enamel microcracks (MCs) on the buccal (a, b) and palatal tooth surface (c, d). Visible MCs, pristine (sound) areas, and tooth surfaces are marked. Panels (a, c) belong to tooth 1, as well as panels (b, d) - to tooth 2.

their legal guardians. All experimental protocols were approved by Vilnius Regional Committee on Biomedical Research Ethics (number 2022/9-1458-933, 28 February 2024). All methods were performed in accordance with the relevant guidelines and regulations. Visibility of the enamel MC [4,22,39] and the pristine locations on the tooth were determined by a specialist dentist (Fig. 2(a–d)).

The presence of enamel MCs visible by the eye was re-confirmed using SEM (Fischer Scientific The Prisma E), operated at 5 kV, 0.18 nA beam current as demonstrated in Fig. 3(a–d). If several cracks were visible on the buccal and palatal surfaces, only one, the longest, was examined. The enamel MCs on the buccal and palatal surfaces of each tooth and pristine area were investigated with X-ray μCT and PL spectroscopy.

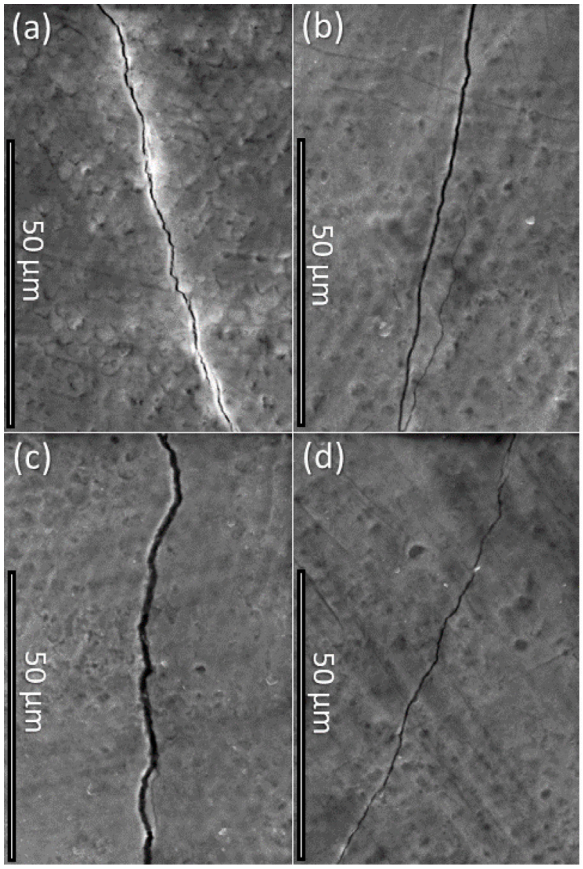

Fig. 3. Typical SEM micrographs of two studied teeth samples with visible enamel microcracks on the buccal (a, b) and palatal tooth surface (c, d). Panels (a, c) belong to tooth 1, as well as panels (b, d) - to tooth 2.

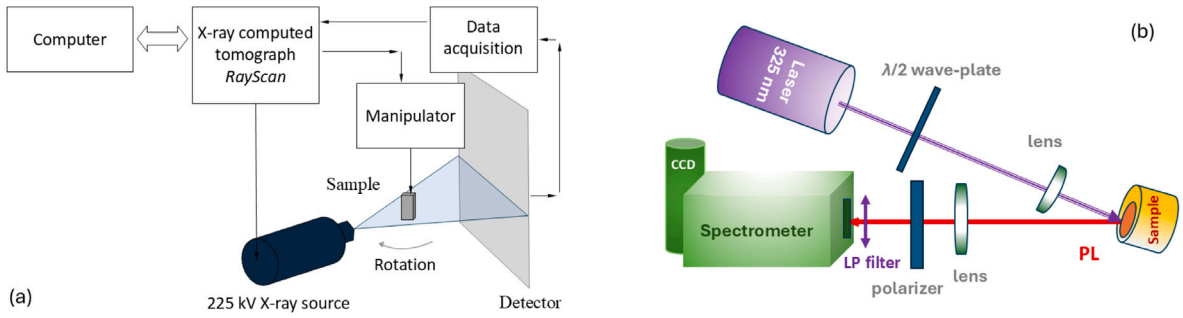

Fig. 4. The experimental setups for (a) an X-ray μCT including the X-ray source, the specimen, and the detector and (b) a PL setup including the laser source, polarization control by $\lambda/2$ waveplate, the tooth sample, the polarizer, cooled CCD, and the spectrometer.

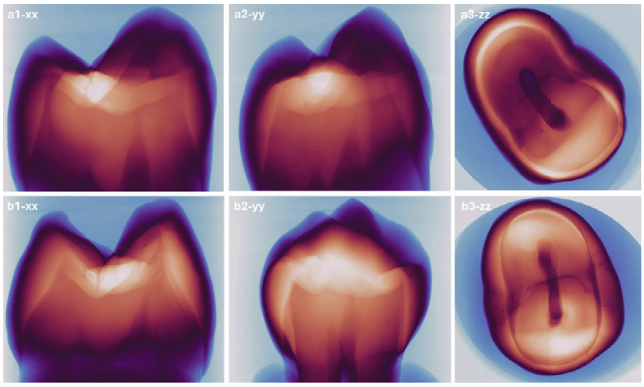

Fig. 5. X-ray μCT datacube projected density map of tooth 1 (a1–a3) and tooth 2 (b1–b3) with visible enamel, dentin, pulp, and cracks. Matplotlib's "twilight" colormap was used to color-code intensity values summed along all three axes shown in columns, respectively.

2.2. X-ray micro-computed tomography (μCT)

2.2.1. Data acquisition

For the scanning procedure, the roots of the teeth samples were embedded in the commercial silicone impression material to hold them mechanically and placed in the medical syringe filled with distilled water (the hydrating medium throughout the study). Investigations were performed using an X-ray 3D μCT RayScan 250E (RayScan Technologies GmbH, Meersburg, Germany). The measurements were carried out employing a microfocus X-ray source with a maximum tube voltage of 225 kV; the tooth samples were scanned at 110 kV. During the measurements, the X-ray source irradiated the sample with the cone beam, and a 2D image at the detector was recorded; the experimental setup is demonstrated in Fig. 4(a). The source-to-sample distance was 50.9 mm while the source-to-detector 1455.1 mm. A flat panel detector with 2048 × 2048 pixels was used. When the sample was rotated throughout 360°, 2970 projections were obtained for each sample. The projections were acquired using 0.5 mm aluminium filter with a 3 s integration time and 3 × averaging, at 80 µA. The focal spot of the X-ray source used was 5 µm, and the size of the resulting voxel was ≈ 7 × 7 × 7 µm^3. Reconstruction of a 3D data set from projections was performed using RayWare software (RayScan Technologies GmbH, Meersburg, Germany). The reconstructed volume size was 1992 × 1992 × 1756 voxels. Dimensional analysis of the buccal and palatal tooth surfaces MCs was carried out with the VGStudio MAX 2023.1 software.

2.2.2. Data preparation for analysis

The custom-made programs were written in Python to process and analyze the 3D data. First, the X-ray images were processed by an intensity threshold operation to identify voxels that lie inside the tooth volume. Next, a 3D mesh structure was created to enclose the volume. This mesh coincides with the outer surface of the enamel of the tooth. Then, a visual image of the tooth with a laser spot on its surface was over-plotted with the mesh, and the mesh was interactively rotated, shifted, and scaled to best match the 2D view of the tooth's shape, i.e., to recover the 3D orientation of the tooth. Finally, the position of the laser spot was marked on the mesh, accurately identifying it in the 3D X-ray datacube. Each position is plotted as a red circle in cube slices.

X-ray slice plots were generated by loading and processing data from the datacube. Specific z coordinate slices were extracted based on predefined coordinates corresponding to the laser spot position, determined via surface mesh. Voxel masks were created from the thresholded data using the scipy.ndimage library[1] to identify the tooth's volume. The largest connected component was isolated as the primary mask of the tooth. For 3D visualization, the skimage.measure library's[2] marching cubes algorithm generated a mesh from the mask data, which was exported as an OBJ file using the trimesh library.[3] Matplotlib[4] was employed to plot and save X-ray slices.

Datacube projections of X-ray samples (tooth 1, Fig. 5(a1–a3) and tooth 2, Fig. 5(b1–b3)) were created by summing data along each axis (z, y, x) using the "twilight" colormap.[5] For slice analysis, X-ray data for specified points of interest were loaded, and slices perpendicular to the z axis were extracted and averaged. Two methods were used for visualization: a simple slice around the z coordinate, and a multi-channel image created by averaging slices at multiple offsets around the z coordinate.

The 3D mesh of a tooth was visualized using the vispy library[6] to identify surface points of interest (laser spot position). The mesh data, loaded from an OBJ file with vispy.io.read-mesh, were used to construct a mesh visual. The mesh was centered and oriented within the image with transformation matrices for accurate spatial representation. A background image, which is an image of tooth with laser point illuminated, was loaded and with applied transparency that allowed simultaneous visualization of the mesh over the experimental view. The mesh was shifted and rotated interactively to match 2D representation of the mesh on the image, allowing to identify laser's spot position on the surface of the tooth. Once the position of the spot was identified on the tooth surface, a slice corresponding to z coordinate was extracted from datacube, and x, y position of the laser spot was indicated by yellow circle on the slice.

[1] https://docs.scipy.org/doc/scipy/reference/ndimage.html
[2] https://scikit-image.org/docs/stable/api/skimage.measure.html
[3] https://trimesh.org/
[4] https://matplotlib.org/
[5] https://matplotlib.org/3.3.3/tutorials/colors/colormaps.html
[6] https://vispy.org/

This mesh-to-image alignment is an interactive rigid adjustment with 4 degrees of freedom (scale, the in-plane x and y position, and the pitch and roll angles), in which the mesh is adjusted until its projected outline coincides with the tooth contour in the optical image. The spatial registration uncertainty of the method is bounded by the laser spot size (diameter ≈ 80 μm) and the μCT voxel size ($\approx 7 \times 7 \times 7$ μm^3), both of which are smaller than the ≈ 1 mm spacing between adjacent measurement points, ensuring that crack-affected and pristine regions are unambiguously distinguished.

2.3. Photoluminescence measurements

2.3.1. Data acquisition

The photoluminescence spectra were obtained using a self-built system with a spectrograph (ACTON 500) and a CCD (PRINCETON Instruments) cooled with liquid nitrogen. The general layout of the experiment, including the laser source, the sample, the cooled CCD, and the spectrometer, is shown in Fig. 4(b). The measurements were carried out using a continuous-wave (cw) laser at 325 nm excitation. The focused beam spot size (diameter) was ≈ 80 μm corresponding to a power density of 0.1 kW/cm^2. For all spectra, the same exposure time of 0.2 s was used. The beam coming out of the laser was polarized (ratio > 100:1, vertical matching with the direction of the crack). A $\lambda/2$ wave-plate was used to control it for the PL measurements by setting it to 0°, 22.5°, 45°, 67.5° in order to obtain 0°, 45°, 90°, and 135° polarizations of the incident beam at the focal spot. Additionally, a rotating polarizer prior to CCD was used to select the 0°, 45°, 90°, 135° polarizations of the luminescent signal. The angle of incidence of the beam with respect to the tooth surface was $\simeq 20°$ and the elongation of the spot size was not crucial ($\leq 10\%$, estimated to be ≈ 85 μm). It is noted that the exact angle of incidence was not important for the PL measurements. Calibration using an integrating sphere was not applied due to its complexity and because it is not common in PL practice.

The tooth was fixed on an x-y-z positional stage mounted on a rotational stage. Three measurement points were spaced equidistantly by 1 mm from each other, and the PL spectrum was registered at each measurement point along the crack line. The same three measurement points were selected for the pristine tooth area, maintaining the same vertical position but with an equal horizontal distance of $\approx$ 1–2 mm between measurement points from the sound and cracked tooth areas by slightly rotating the tooth to trace the crack. The same procedure was repeated for the buccal and palatal tooth surfaces.

In total, 192 PL spectra were detected for each sample: 96 from visible enamel MCs from the buccal and palatal surfaces, and 96 from the pristine areas from the buccal and palatal surfaces.

2.3.2. Data preparation for analysis

The custom-made programs were written in Python to process raw spectra, perform identification of defects (e.g., lines), median smoothing, normalization, and averaging of the spectral data.

The spectral flux data were corrected to mitigate noise and anomalies, thereby ensuring reliable interpretation of the spectral signatures. Initially, a median filter from the SciPy library was applied to the flux data extracted from .SPE files using the WinSpec software.[7] This filtering involved replacing each data point with the median value within a specified window size. Outliers, identified where the deviation between original and filtered data exceeded a set threshold, were expanded to include adjacent points. These outliers were then replaced by median-filtered values, with a small amount of locally-matched noise added (NumPy[8]) so that the corrected points were consistent with the surrounding data. These changes were cosmetic and did not affect the spectral shape or subsequent analysis. A further median filtering refined the flux data. The corrected flux was normalized by integrating over a defined wavelength range to facilitate consistent comparison. Matplotlib was utilized to plot the normalized data, with spectra for 'good' and 'crack' points distinguished by color.

Each individual spectrum was smoothed by 5 nm median window sliding filter to remove the laser light from the spectrum. Each individual line corresponded to a single measurement obtained at specific polarizer and analyzer orientation angles (6 good and 6 crack spots per tooth at 4 polarizer and 4 analyzer angles - a total of 192 spectra per tooth). For each tooth the average spectrum was computed for pristine and cracked areas, averaging over different polarization angle spectra to increase signal-to-noise (S/N) ratio.

To quantify the spectral-shape difference between pristine and cracked regions, a peak asymmetry index (PAI) was defined as the ratio of the normalized emission intensity at the two characteristic maxima, PAI = I(444 nm)/I(530 nm). For each measurement point, the PAI was computed from the polarization-averaged, area-normalized spectrum, yielding one value per point (six cracked and six pristine points per tooth). Group means were compared using a two-sample t-test. A non-parametric Mann–Whitney U test was also performed to confirm robustness at the small sample size.

2.4. Energy-dispersive X-ray spectroscopy analysis

Energy-dispersive X-ray spectroscopy (EDS) analysis was performed using a Hitachi TM3000 SEM. Elemental analysis was conducted at an accelerating voltage of 15 kV, with a sample acquisition time of 300 s. The elemental composition in both pristine and cracked regions was determined from three measurements per region acquired at the points indicated in the images (see Suppl. Fig. S1).

3. Results

3.1. Characterization of microcracks using μCT

The scanning technique allowed the recognition, detection and 3D characterization of all tooth MCs, accurately identifying those cracks that were later analyzed using PL. MCs that were visible on the outer buccal and palatal surfaces and re-confirmed with SEM were clearly distinguished from the surrounding pristine tooth areas. The dynamics of the cracks from the outer enamel surface to the deeper tooth structures were evaluated, as well as the MCs' direction and position with respect to the DEJ. The convexity of the buccal and palatal premolar surfaces, the width of the enamel layer, and the scanning of the samples in a hydrated environment, did not prevent the identification and assessment of the crack of interest (tooth 1, Fig. 5(a1–a3) and tooth 2, Fig. 5(b1–b3)).

3.2. Spectral analysis of microcracks with PL

The results of the PL spectra of the cracked and pristine areas of the buccal and palatal surfaces of both samples using a 325 nm laser are shown in Fig. 6. The photoluminescence spectra of both tooth 1 (Fig. 6(a)) and tooth 2 (Fig. 6(b)) reveal systematic differences between the pristine (blue lines) and cracked areas (red lines). Each individual spectrum features two distinct peaks, with the left-side peak in the pristine spectra being slightly more intense than the right-side peak. This asymmetry is not as pronounced in the cracked regions, indicating a potential alteration in the material properties in the cracking areas. To better illustrate the systematic difference, the mean value of cracked area spectra is plotted as a yellow line, and the mean value of pristine area spectra is plotted as a cyan line. The consistent difference between the cracked and pristine areas across both samples suggests a structural or compositional change associated with crack formation. Clarifying whether this alteration is a consequence or a cause of cracking remains the subject of further investigation.

[7] https://github.com/antonl/pyWinSpec
[8] https://numpy.org/

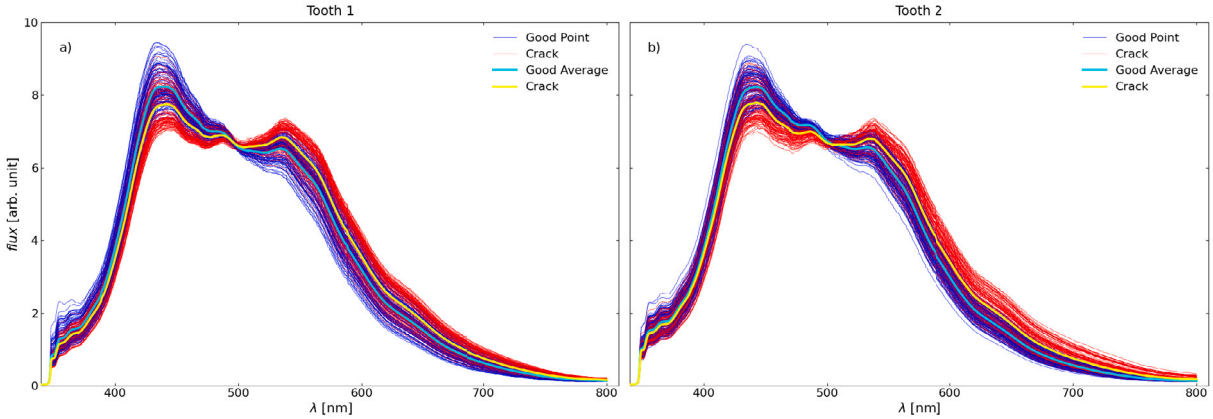

Fig. 6. PL spectra of the cracked (red) and pristine (blue) areas of the buccal and palatal surfaces of tooth 1 (a) and tooth 2 (b) with a 325 nm laser excitation (x axis - wavelength (nm), y axis - normalized intensity (arbitrary units)). Cyan and yellow lines show the mean spectra of pristine and cracked regions, respectively.

To quantify this difference, the PAI = I(444 nm)/I(530 nm) was evaluated for each measurement point. The PAI was lower in cracked than in pristine regions in both teeth (tooth 1: 1.16 ± 0.12 *vs* 1.29 ± 0.13; tooth 2: 1.16 ± 0.11 *vs* 1.26 ± 0.10), with the reduced left-peak dominance reproduced independently in each specimen. Pooling the measurement points across both teeth (n = 12 per group), the difference was statistically significant (1.16 ± 0.11 *vs* 1.28 ± 0.11; p = 0.014, two-sample t-test; Mann–Whitney U test p = 0.046; Cohen's d ≈ 1.1, a large effect; ≈ 9% relative reduction).

3.3. Optical, X-ray and PL spectral mapping

Images of an optical view of three measurement points of the good and cracked tooth areas, both on the buccal and palatal tooth surfaces are presented in the first column of Fig. 7 (points (**1–12**) - tooth 1) and Fig. 8 (points (**1–12**) - tooth 2). Each measurement point corresponds to the different third of the buccal and palatal tooth surface (occlusal, middle, and cervical). The white dot shows the area of interest that has been accurately identified and mapped on the X-ray images (second column, yellow circle), zoom-in onto the measurement position (third column), and the spectra analysis performed on this location (fourth column). X-ray images are positioned at the same rotation angle as optical images.

In the μCT slice views, the color-coding represents a color-coded distance from the viewer along the slice: red color is a mean of 9 slices further along the z axis, green is the mean of 9 slices on exactly the slice where the laser was pointing, and blue is the mean of 9 slices closer (Fig. 7 (points (**1–12**) - tooth 1) and Fig. 8 (points (**1–12**) - tooth 2)). The mean of slices gives a better signal-to-noise ratio to enhance the view of faint cracks, while distance color-coding indicates if the crack is parallel to the axis of slicing or slightly tilted.

3.4. Elemental analysis of microcracks using EDS

The main results of EDS measurements are shown in Table 1. Elemental composition in both uncracked and cracked regions was averaged over defined measurement points marked in the micrographs (see Suppl. Fig. S1). The cracked regions contained more carbon than the pristine (good) areas (36.9 ± 13.5 at.% *vs* 26.0 ± 7.4 at.%, Table 1), corresponding to a 42% relative increase in the averaged carbon content and reaching a 1.8-fold increase at individual crack sites (tooth 1, buccal). This higher carbon concentration was accompanied by a decrease in oxygen (56.8 → 44.0 at.%), so that the carbon-to-oxygen ratio rose from 0.46 in the pristine areas to 0.84 in the cracked regions (an 83% relative increase). The calcium and phosphorus contents changed comparatively little between the two areas (Table 1). The larger standard deviations in the cracked regions (e.g., 13.5 *vs* 7.4 at.% for carbon) indicate that the crack-affected regions are compositionally more heterogeneous than the uncracked enamel.

4. Discussion

The current findings demonstrate a measurement methodology for identifying the same cracked and pristine tooth areas by combining X-ray μCT (volumetric analysis) with PL (spectral analysis) through the 3D surface mesh structure developed, with a validated spatial registration linking the two modalities. The small dimensions of the MCs pose a major methodological challenge of locating them with both techniques. The cracks characterized in this study fall within the dimensional ranges reported in the literature [4,22,24–27], and the validated registration — with a spatial uncertainty bounded by the laser spot size (diameter ≈ 80 μm) and the μCT voxel size (≈ 7 × 7 × 7 μm^3) - was sufficient to co-locate them across modalities despite their small size.

Compared to previous works [22,27], in this study MCs were less pronounced in the μCT images. This can be explained by the fact that the teeth samples were kept in a hydrated environment during the entire X-ray μCT scanning. Previously, it could only be assumed that the imaging of teeth with MCs in aqueous solution should be different. It is now known that cracks are still visible and can be identified, but they tend to be less pronounced, and the scanning procedure itself takes longer. The most important point is that the images obtained of teeth with MCs kept in a hydrated environment more closely resemble the clinical situation, as the teeth in the mouth are permanently kept in the aqueous medium. Although MCs were less pronounced, they could still be clearly distinguished from occlusal fissures. Fissures are natural anatomical grooves located on the occlusal surfaces of premolars and molars [40]. Unlike MCs, fissures form during tooth development. Although they do not generally affect the strength of enamel, due to their complex anatomy, fissures can lead to plaque accumulation and caries if not properly maintained [40].

The anatomical (e.g., convexity of the surface) and morphological (e.g., tooth surface irregularity) features of the buccal and palatal tooth surfaces challenged the identification of measurement points for PL analysis. To overcome this, the three measurement points were positioned systematically using the x-y-z stage (Subsection 2.3.1) — at 1 mm spacing along the crack line and at the same vertical position on the pristine side — rather than by visual selection, ensuring reproducible sampling.

As the crack is a gap between enamel crystallites, it is expected to present an altered PL response. It is well-known that tooth PL decreases when mineral content decreases, and the gap is an area without tooth minerals. This relationship is what allows the spectro-spatial properties of the tooth material to be merged. Structural information on the direction of cracks relative to the orientation of crystallites and inter-crystalline pore organic content would be valuable, but this would

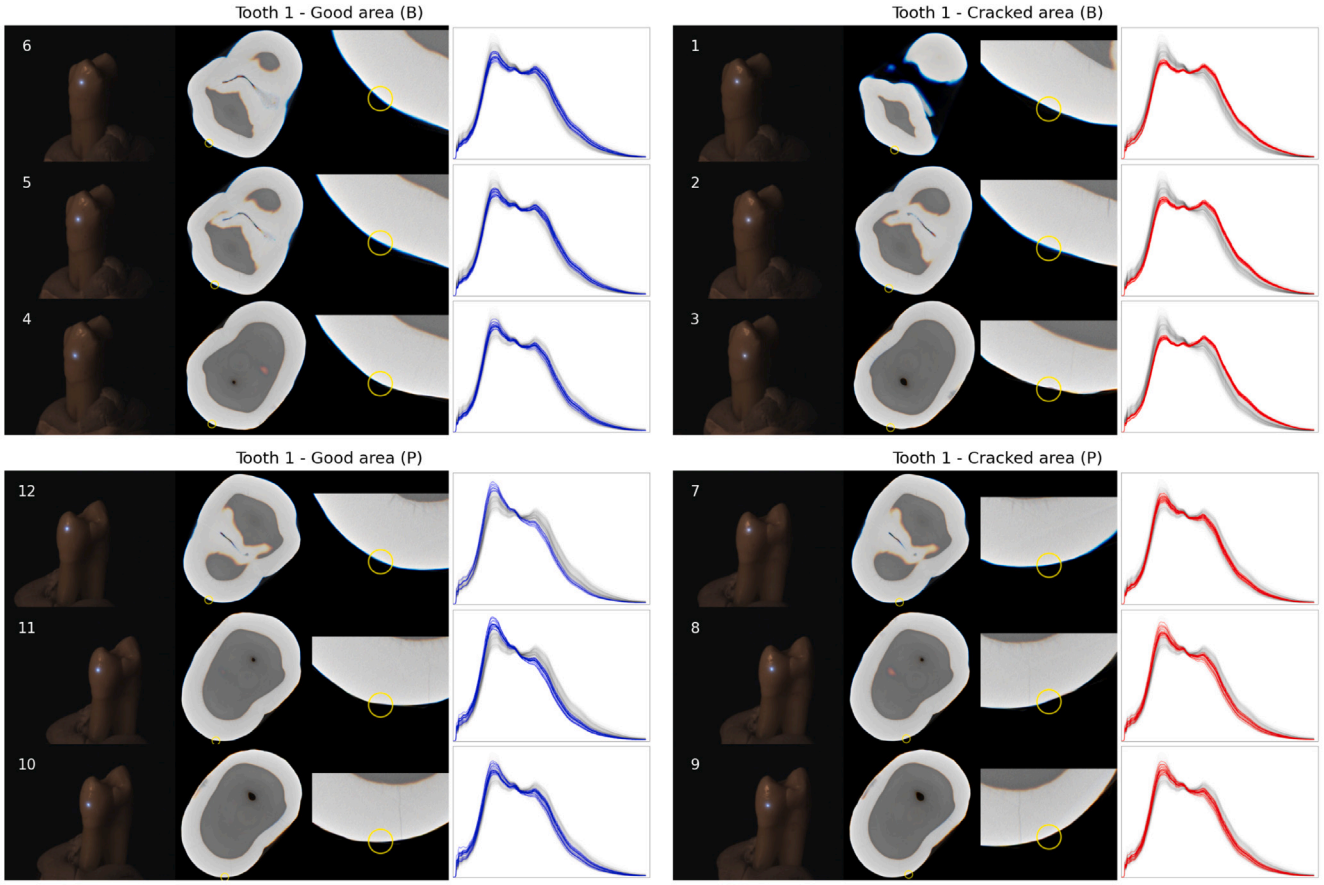

Fig. 7. Correlative mapping of optical view, μCT slices, and PL spectra at twelve measurement points on tooth 1 (excitation at 325 nm). Each row corresponds to one measurement point and shows, from left to right: an optical view with the laser spot (white dot), a μCT slice view with a yellow circle marking the laser position, a zoomed-in slice view, and a colored spectra plot overlaid on the full set of spectra from the tooth. Optical view images, points (1, 6, 7, 12) belong to the occlusal third of both tooth surfaces, either cracked or good areas, points (2, 5, 8, 11) - to the middle third, as well as points (3, 4, 9, 10) - to the cervical third.

Table 1
EDS results are reported in atomic percentages (at.%). The elemental composition in both uncracked and cracked regions was determined from three measurements acquired at the points indicated in the micrographs (see Suppl. Fig. S1). The reported values represent the mean values (Avg.) with corresponding standard deviations (St. Dev.).

Sample	Elements, at. %							
	C		O		P		Ca	
	Avg.	St. Dev.	Avg.	St. Dev.	Avg.	St. Dev.	Avg.	St. Dev.
Tooth 1 good (P)	31.14	0.85	57.49	2.25	5.56	0.63	5.56	1.15
Tooth 1 cracked (P)	25.80	7.64	56.65	1.41	6.22	0.84	6.36	1.61
Tooth 1 good (B)	30.00	3.57	59.44	3.62	5.01	0.23	4.77	0.48
Tooth 1 cracked (B)	55.36	6.73	26.37	3.65	6.64	1.42	11.63	2.06
Tooth 2 good (P)	17.83	2.27	66.06	1.61	7.75	0.63	8.05	0.57
Tooth 2 cracked (P)	38.36	7.70	49.82	6.04	5.20	0.83	5.58	0.91
Tooth 2 good (B)	24.82	1.53	44.18	0.49	12.68	0.88	17.90	1.24
Tooth 2 cracked (B)	27.93	0.87	43.11	3.50	9.31	4.50	17.36	3.52
Mean of good	25.95	7.38	56.79	4.49	8.73	3.49	9.07	6.05
Mean of cracked	36.86	13.50	43.99	12.98	6.84	1.75	10.24	5.46
Difference in mean	−10.91		12.80		1.89		−1.17	

require higher-resolution electron microscopic analysis. Photoluminescence polarization analysis can be used for the determination of the anisotropy of the emitting species. The energy deposition (excitation) is due to the dichroism in absorption as well as birefringence (cause reflection anisotropy and polarization rotation in the sample). It can be measured from the four polarization (4-pol.) mapping using optical far [41] (propagating) and even near [42] (non-propagating) fields. It is noteworthy that this 4-pol. mapping can distinguish alignment and anisotropy in absorption/transmission up to 20 times below the diffraction limit, which would correspond to ≈ 2 μm features in these PL studies [43].

The spectroscopic examination demonstrates significant differences in PL spectral shape between cracked and pristine enamel. The peak asymmetry index decreased from 1.28 ± 0.11 in pristine regions to

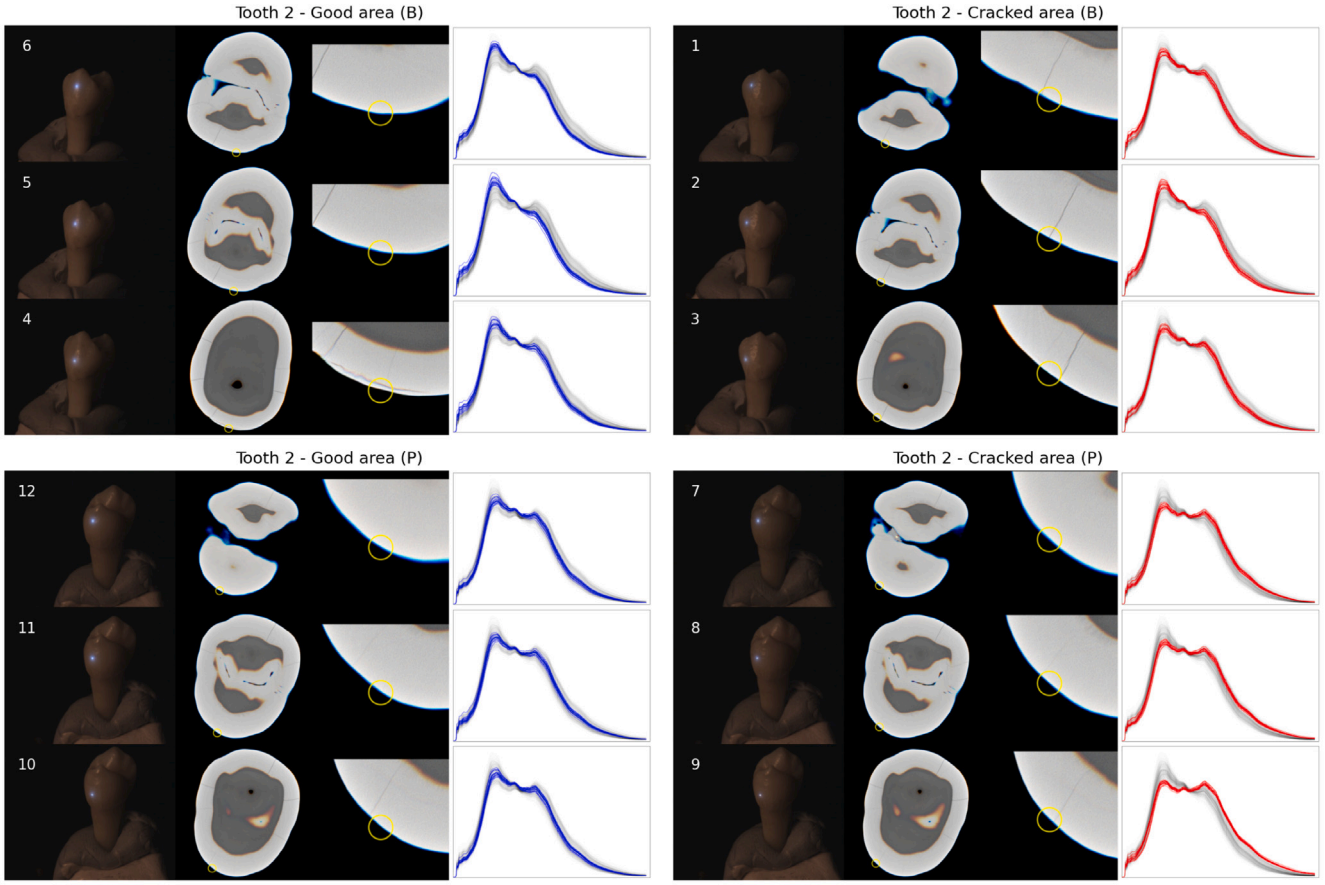

Fig. 8. Correlative mapping of optical view, μCT slices, and PL spectra at twelve measurement points on tooth 2 (excitation at 325 nm; same as for Fig. 7).

1.16 ± 0.11 in cracked regions (pooled across both teeth; p = 0.014, Cohen's d ≈ 1.1), confirming that the change in spectral shape is reproducible and quantifiable. Analyzing the intensity spectra by distinguishing the excitation to discrete 0° and 90° as well as detection 0° and 90°, polarization-sensitive luminescence is observed in all the cases (buccal and palatal surfaces, pristine and cracked areas; see Suppl. Fig. S2 (exemplified case of Fig. 7, point 8 and point 11)). The more effective energy deposition (absorption) occurs when polarization is in line with the longitudinal axis of the tooth (V-vertical), as seen in Suppl. Fig. S2(a) and (b). The effect can be attributed to the orientation of the crystal rods (prisms), which extend in a nearly parallel manner in the enamel closest to the tooth surface [2]. The orientation of the enamel rods (prisms) causes anisotropy of the luminescence — the intensity of the excitations decreases with a shift to perpendicular (H-horizontal) polarization (90°). Furthermore, it decreases significantly once the polarizer is turned from vertical to horizontal (both VH and HH), enabling polarization selective registration. This supports the claim for polarization dichroism, namely irradiation by vertically (0°) polarized light being more efficiently absorbed due to matching orientation with the crystal rods (prisms), disregarding the crack itself (see Suppl. Fig. S2 (a)). However, the horizontal (90°) polarization is still absorbed efficiently due to light penetrating deeper below the surface, reaching the more randomly oriented prisms [2]. Although MCs do not fall into the category of carious lesions, the differences in the PL spectra suggest that structural changes occur at the crack site.

This interpretation is consistent with the behavior of demineralized enamel. In the presence of caries damage (at pH < 5.5), enamel demineralization occurs, i.e., HAP dissolves [44]. The inorganic substances are being removed by the oral acids, produced by oral bacteria, resulting in a porous enamel structure and light-to-dark colored cavities on the surface [32]. During the initial stages of caries, the tooth structure is intact [32]. However, as carious lesion worsens, the tooth becomes porous due to demineralization and shows lower mineral concentration [32]. In such case, the fluorescence intensity from the minerals decreases along with the reduced light transmission, as dark areas absorb more light than lighter-colored regions [32]. Also, the inhomogeneous porous structure increases the scattering of transmitted light [32]. In the context of PL excitation, this is expected to cause a less intense and differently shaped PL emission — consistent with the reduced peak asymmetry we measure at the crack sites.

The EDS measurements provide an independent, compositional confirmation of this picture. The cracked regions showed an increase in carbon content compared to the pristine areas (36.9 ± 13.5 at.% *vs* 26.0 ± 7.4 at.%; a 42% relative increase, reaching a 1.8-fold increase at individual crack sites), accompanied by a decrease in oxygen, so that the carbon-to-oxygen ratio rose from 0.46 (pristine enamel) to 0.84 (cracked enamel; as presented in more detail in the Results section). This shift from mineral-dominated to a more carbon-rich composition is consistent with the accumulation of organic substances — such as proteins, lipids, or bacterial biofilm residues, which are rich in carbon — within the crack [45], and with the demineralization process that usually accompanies carious or non-carious defects such as white spot lesions. When tooth material begins to decay, the calcium [35] and phosphorus content decreases [36], while the relative carbon concentration increases [37]. EDS studies of demineralized enamel have also demonstrated the loss of minor elements, leading to a less diverse EDS spectrum without sodium, magnesium, and chlorine elements, which are typically found in good enamel areas [36]. Although these minor elements were not quantified in the present analysis, the carbon increase we observe follows that reported trend. Our elemental analysis is consistent with previous EDS studies performed on demineralized tooth surfaces after sectioning [35–37] and confirms a similar tendency.

What distinguishes the present work methodologically is that the EDS was carried out non-destructively on the intact tooth with a not-flat surface, avoiding sectioning, thereby providing a more representative view of enamel chemistry in the cracked regions and preserving the structural integrity of the sample.

It is important to mention that the compositional changes between pristine and crack-affected enamel regions coincide with the spectral-shape change observed in Fig. 6 and quantified by the PAI (1.16 in cracked, *vs* 1.28 in pristine regions, pooled across both teeth). Specifically, crack-associated regions exhibit reduced relative emission near 444 nm and a higher relative contribution in the 480–600 nm region, i.e., a lower PAI. The correlation between increased carbon concentration and the modified PL response suggests that crack formation is associated not only with structural discontinuities but also with local chemical alterations. Increased carbon content reflects the accumulation of organic material or localized demineralization, both of which can change light absorption, scattering, and non-radiative relaxation pathways [46], thereby influencing the luminescence response.

The small sample size could be considered as one of the main limitations of the current study. However, the number of specimens does not directly limit the number of measurements: 192 PL spectra were acquired per tooth at twelve precisely identified points, and the same points were extracted from the reconstructed 3D X-ray data using the mesh structure created to coincide with the enamel contour, giving more than 200 PL and X-ray measurements per sample and more than 400 across the study. With six cracked and six pristine points within a single tooth, the per-tooth PAI comparisons do not individually reach significance (tooth 1: $p = 0.086$, tooth 2: $p = 0.120$). However, pooling the measurement points across both teeth ($n = 12$ per group) yields a statistically significant difference ($p = 0.014$) with a large effect size (Cohen's $d \approx 1.1$). The same direction and magnitude of the effect appeared in both teeth, and together with the significant pooled result, this supports the PAI as a reproducible measure of the spectral difference between cracked and pristine regions. A larger sample size will be needed to confirm the generality of this result and to assess the repeatability and reproducibility of the combined measurement chain.

Taken together, the advances of this work are methodological. The validated 3D surface mesh-assisted registration links volumetric μCT and PL on an intact specimen with a co-localization bounded by the laser spot size (diameter ≈ 80 μm) and the μCT voxel size ($\approx 7 \times 7 \times 7$ μm^3). This explicit identification of registration uncertainty, together with the PAI, provides a reproducible measure of the spectral difference between cracked and pristine enamel, supported by complementary EDS evidence of compositional changes. Demonstrated here on tooth enamel, the methodology is, by design, applicable to other heterogeneous mineralized and composite materials that require correlative volumetric and spectroscopic defect characterization.

5. Conclusions and outlook

Correlative characterization of micro-scale defects in heterogeneous mineralized materials requires linking measurement modalities that differ in resolution, contrast mechanism, and coordinate system.

To address this, a 3D mesh structure overlapping the outer enamel surface of the tooth was created, bridging the 3D X-ray and spectral images so that the same cracked and pristine areas could be identified across modalities. The methodology was demonstrated on extracted human premolars with enamel cracks, using X-ray μCT and PL as the co-registered modalities and complementary EDS for compositional characterization. The registration links the two modalities with a spatial uncertainty bounded by the laser spot size (diameter ≈ 80 μm) and the μCT voxel size ($\approx 7 \times 7 \times 7$ μm^3). The presented protocol can be applied to all the teeth's microstructure and surface mapping analysis, irrespective of tooth group or MC's characteristics and position. Orientation of the sample is key information for comparison between different imaging and spectroscopy techniques based on polarization of light as well as X-rays.

Using this framework, a new important finding is that when analyzing the intensity of normalized spectra, the shape of the spectra changed, allowing determination of which part of the tooth it was registered — cracked *vs* pristine. This change in spectral shape, quantified by the PAI (1.16 in cracked *vs* 1.28 in pristine regions, pooled across both teeth), was statistically significant ($p = 0.014$, Cohen's $d \approx 1.1$). Thus, this empowers reverse spectro-spatial identification of the damaged area by judging from the obtained PL spectrum. The observed spectral variations are consistent with elemental differences between cracked and good areas — in particular a relative increase in carbon content at the crack sites (a 42% increase in the averaged values; carbon-to-oxygen ratio rising from 0.46 to 0.84) — revealing an underlying connection between composition and optical response. To our knowledge, this is the first non-destructive study of such correlations in the entire tooth. This integrated multispectral approach improves the detection and characterization of MCs by offering a validated methodology for assessing enamel integrity along cracks, combining structural, optical, and elemental analysis.

Several outlook directions are opened by the validated framework. A key limitation of the current implementation is the μCT voxel size ($\approx 7 \times 7 \times 7$ μm^3), which sets a lower bound on the smallest crack width that can be reliably detected. Higher-resolution X-ray imaging techniques, such as lens-based X-ray microscopy and synchrotron nano-CT [47], would lower the detection limit and enable determination of crack-tip geometry and the structure of the enamel prism surface. Since this mesh-assisted registration operates on the outer surface rather than on voxel data directly, the same procedure can be applied without modification to meshes generated from higher-resolution μCT data. On the spectroscopic side, Raman microspectroscopy [48] registered through the same mesh framework would provide molecular specificity and allow independent verification of the interpretation of organic infiltration. Because the PL measurement is point-resolved and surface-accessible, it is compatible with miniaturized fiber-optic probes, opening the way for *in vivo* applications once optical-environment challenges (e.g., saliva, biofilms, restorations) are addressed. When a sufficiently large dataset is available, the validated spectra may also support data-driven spectral classification; such methods are foreseen as future extensions, evaluated under the same metrological criteria, rather than as components of the current methodology. Longitudinal research assessing the effectiveness of crack remineralization therapy, guided by the diagnostic accuracy provided by our combined X-ray μCT and PL approach, would be invaluable in translating these findings into clinical practice.

CRediT authorship contribution statement

Irma Dumbryte: Writing – review & editing, Writing – original draft, Visualization, Project administration, Funding acquisition, Formal analysis, Conceptualization. **Donatas Narbutis:** Writing – review & editing, Writing – original draft, Visualization, Formal analysis, Data curation, Conceptualization. **Maria Androulidaki:** Writing – review & editing, Writing – original draft, Visualization, Formal analysis, Data curation. **Edvinas Skliutas:** Writing – review & editing, Formal analysis, Data curation. **Robertas Virketis:** Writing – review & editing, Validation, Formal analysis, Data curation. **Elena Jasiuniene:** Writing – review & editing, Writing – original draft, Formal analysis, Data curation. **Saulius Juodkazis:** Writing – review & editing, Writing – original draft, Data curation, Conceptualization. **Greta Merkininkaite:** Writing – review & editing, Formal analysis, Data curation. **Mangirdas Malinauskas:** Writing – review & editing, Writing – original draft, Project administration, Data curation, Conceptualization.

Declaration of generative AI and AI-assisted technologies in the manuscript preparation process

During the preparation of this work, the authors used Claude (claude.ai) in order to improve the language and readability of the manuscript. After using this tool, the authors reviewed and edited the content as needed and take full responsibility for the content of the published article.

Declaration of competing interest

The authors declare that they have no known competing financial interests or personal relationships that could have appeared to influence the work reported in this paper.

Acknowledgments

This project has received funding from the Research Council of Lithuania (LMTLT), agreement No S-ITP-25-6.

This research has received financial support from the European Union's Horizon 2020 research and innovation programme under grant agreement No 101007417 having benefited from the access provided by FORTH - Foundation for Research and Technology Hellas access provider in Heraklion, Crete (EL) access site within the framework of the NFFA-Europe Pilot Transnational Access Activity, proposal ID-572.

Appendix A. Supplementary data

Supplementary material related to this article can be found online at https://doi.org/10.1016/j.measurement.2026.122366.

Data availability

The data supporting this article has been included as part of the Supplementary Material.

References

[1] M.F. Little, F.S. Casciani, The nature of water in sound human enamel. A preliminary study, Arch. Oral. Biol. 11 (1966) 565–571, http://dx.doi.org/10.1016/0003-9969(66)90222-6.

[2] D. Bajaj, S. Park, G.D. Quinn, D. Arola, Fracture processes and mechanisms of crack growth resistance in human enamel, J. Min. Met. Mat. S. 62 (7) (2010) 76–82, http://dx.doi.org/10.1007/s11837-010-0113-8.

[3] S. Habelitz, S.J. Marshall, G.W. Marshall, Jr., M. Balooch, Mechanical properties of human dental enamel on the nanometre scale, Arch. Oral. Biol. 46 (2) (2001) 173–183, http://dx.doi.org/10.1016/S0003-9969(00)00089-3.

[4] I. Dumbryte, Evaluation of enamel microcracks' characteristics before and after removal of metal and ceramic brackets for teeth from younger- and older-age groups: an in vitro study (Ph.D. thesis), Vilnius University, 2020, http://dx.doi.org/10.13140/RG.2.2.13161.65120.

[5] E. Beniash, C.A. Stifler, C.Y. Sun, G.S. Jung, Z. Qin, M.J. Buehler, P.U. Gilbert, The hidden structure of human enamel, Nat. Commun. 10 (1) (2019) 4383, http://dx.doi.org/10.1038/s41467-019-12185-7.

[6] H.J. Orams, Visualisation of micropore structure in human dental enamel, Nature 252 (5484) (1974) 584–585, http://dx.doi.org/10.1038/252584a0.

[7] S. Habelitz, Materials engineering by ameloblasts, J. Dent. Res. 94 (2015) 759–767, http://dx.doi.org/10.1177/0022034515577963.

[8] L. Shen, F. Barbosa de Sousa, N.B. Tay, T.S. Lang, V.L. Kaixin, J. Han, L.T. Kilpatrick-Liverman, W. Wang, S. Lavender, S. Pilch, H.Y. Gan, Deformation behavior of normal human enamel: A study by nanoindentation, J. Mech. Behav. Biomed. Mater. 108 (2020) 103799, http://dx.doi.org/10.1016/j.jmbbm.2020.103799.

[9] U.G.K. Wegst, H. Bai, E. Saiz, A.P. Tomsia, R.O. Ritchie, Bioinspired structural materials, Nat. Mater. 14 (1) (2015) 23–36, http://dx.doi.org/10.1038/nmat4089.

[10] V. Imbeni, J.J. Kruzic, G.W. Marshall, S.J. Marshall, R.O. Ritchie, The dentin-enamel junction and the fracture of human teeth, Nat. Mater. 4 (3) (2005) 229–232, http://dx.doi.org/10.1038/nmat1323.

[11] M. Mirkhalaf, A.K. Dastjerdi, F. Barthelat, Overcoming the brittleness of glass through bio-inspiration and micro-architecture, Nat. Commun. 5 (2014) 3166, http://dx.doi.org/10.1038/NCOMMS4166.

[12] B.U. Zachrisson, O. Skogan, S. Höymyhr, Enamel cracks in debonded, debanded, and orthodontically untreated teeth, Am. J. Orthod. 77 (3) (1980) 307–319, http://dx.doi.org/10.1016/0002-9416(80)90084-6.

[13] M. Abou-Rass, Crack lines: the precursors of tooth fractures - their diagnosis and treatment, Quintessence Int. Dent. Dig. 14 (4) (1983) 437–447, http://europepmc.org/abstract/MED/6574554.

[14] H.H.K. Xu, J.R. Kelly, S. Jahanmir, V.P. Thompson, E.D. Rekow, Enamel subsurface damage due to tooth preparation with diamonds, J. Dent. Res. 76 (10) (1997) 1698–1706, http://dx.doi.org/10.1177/00220345970760101201.

[15] I. Dumbryte, T. Jonavicius, L. Linkeviciene, T. Linkevicius, V. Peciuliene, M. Malinauskas, Enamel cracks evaluation – A method to predict tooth surface damage during the debonding, Dent. Mater. J. 34 (6) (2015) 828–834, http://dx.doi.org/10.4012/dmj.2015-085.

[16] B.A. Lloyd, M.B. McGinley, W.S. Brown, Thermal stress in teeth, J. Dent. Res. 57 (4) (1978) 571–582, http://dx.doi.org/10.1177/00220345780570040701.

[17] I. Dumbryte, J. Vebriene, L. Linkeviciene, M. Malinauskas, Enamel microcracks in the form of tooth damage during orthodontic debonding: a systematic review and meta-analysis of *in vitro* studies, Eur. J. Orthod. 40 (6) (2018) 636–648, http://dx.doi.org/10.1093/ejo/cjx102.

[18] F.M.F. Kitahara-Céia, J.N. Mucha, P.A.M. dos Santos, Assessment of enamel damage after removal of ceramic brackets, Am. J. Orthod. Dentofacial. Orthop. 134 (4) (2008) 548–555, http://dx.doi.org/10.1016/j.ajodo.2006.08.022.

[19] M. Shahabi, F. Heravi, N. Mokhber, R. Karamad, S.E. Bishara, Effects on shear bond strength and the enamel surface with an enamel bonding agent, Am. J. Orthod. Dentofacial. Orthop. 137 (3) (2010) 375–378, http://dx.doi.org/10.1016/j.ajodo.2008.03.030.

[20] M. Habibi, T.H. Nik, T. Hooshmand, Comparison of debonding characteristics of metal and ceramic orthodontic brackets to enamel: an *in-vitro* study, Am. J. Orthod. Dentofacial. Orthop. 132 (5) (2007) 675–679, http://dx.doi.org/10.1016/j.ajodo.2005.11.040.

[21] O. Sorel, R. El Alam, F. Chagneau, G. Cathelineau, Comparison of bond strength between simple foil mesh and laser-structured base retention brackets, Am. J. Orthod. Dentofacial. Orthop. 122 (3) (2002) 260–266, http://dx.doi.org/10.1067/mod.2002.125834.

[22] I. Dumbryte, A. Vailionis, E. Skliutas, S. Juodkazis, M. Malinauskas, Three-dimensional non-destructive visualization of teeth enamel microcracks using X-ray micro-computed tomography, Sci. Rep. 11 (1) (2021) 14810, http://dx.doi.org/10.1038/s41598-021-94303-4.

[23] I. Dumbryte, D. Narbutis, M. Androulidaki, A. Vailionis, S. Juodkazis, M. Malinauskas, Teeth microcracks research: Towards multi-modal imaging, Bioengineering 10 (12) (2023) 1354, http://dx.doi.org/10.3390/bioengineering10121354.

[24] K. Sun, L. Yuan, Z. Shen, Z. Xu, Q. Zhu, X. Ni, J. Lu, Scanning laser-line source technique for nondestructive evaluation of cracks in human teeth, Appl. Opt. 53 (11) (2014) 2366–2374, http://dx.doi.org/10.1364/AO.53.002366.

[25] Z. Li, Y.V. Holamoge, Z. Li, W. Zaid, M.L. Osborn, A. Ramos, J.T. Miller, Y. Li, S. Yao, J. Xu, Detection and analysis of enamel cracks by ICG-NIR fluorescence dental imaging, Ann. New York Acad. Sci. 1475 (1) (2020) 52–63, http://dx.doi.org/10.1111/nyas.14374.

[26] M.O. Culjat, R.S. Singh, E.R. Brown, R.R. Neurgaonkar, D.C. Yoon, S.N. White, Ultrasound crack detection in a simulated human tooth, Dentomaxillofac. Radiol. 34 (2) (2005) 80–85, http://dx.doi.org/10.1259/dmfr/12901010.

[27] I. Dumbryte, D. Narbutis, A. Vailionis, S. Juodkazis, M. Malinauskas, Revelation of microcracks as tooth structural element by X-ray tomography and machine learning, Sci. Rep. 12 (1) (2022) 22489, http://dx.doi.org/10.1038/s41598-022-27062-5.

[28] Ossila, Photoluminescence (PL) spectroscopy, 2023, https://www.ossila.com/pages/photoluminescence.

[29] C.A.M. Volpato, M.R.C. Pereira, F.S. Silva, Fluorescence of natural teeth and restorative materials, methods for analysis and quantification: A literature review, Esthet. Restor. Dent. 30 (5) (2018) 397–407, http://dx.doi.org/10.1111/jerd.12421.

[30] Y.-K. Lee, Fluorescence properties of human teeth and dental calculus for clinical applications, J. Biomed. Opt. 20 (4) (2015) 040901, http://dx.doi.org/10.1117/1.JBO.20.4.040901.

[31] A.A.-R.S. Marouf, Y.A. Khairallah, E.M. Awooda, Photoemission spectra of sound tooth and those of different carious stages, Eur. Biophys. J. 7 (1) (2019) 23–26, http://dx.doi.org/10.11648/j.ejb.20190701.14.

[32] C.-C. Ko, D.-H. Yi, D.J. Lee, J. Kwon, F. Garcia-Godoy, Y.H. Kwon, Diagnosis and staging of caries using spectral factors derived from the blue laser-induced autofluorescence spectrum, J. Dent. 67 (2017) 77—83, http://dx.doi.org/10.1016/j.jdent.2017.09.015.

[33] A. Mahmoud, S. Elbasuney, Y.H. El-Sharkawy, Instant identification of dental white spot using K-means algorithm via laser-induced fluorescence and associated hyperspectral imaging, J. Photochem. Photobiol. B, Biol. 245 (2023) 112749, http://dx.doi.org/10.1016/j.jphotobiol.2023.112749.

[34] T.M.F. Caneppele, C. Rocha Gomes Torres, E. Bresciani, Analysis of the color and fluorescence alterations of enamel and dentin treated with hydrogen peroxide, Braz. Dent. J. 26 (5) (2015) 514—518, http://dx.doi.org/10.1590/0103-6440201300249.

[35] C. Besnard, R.A. Harper, E. Salvati, T.E. Moxham, L. Romano Brandt, G. Landini, R.M. Shelton, A.M. Korsunsky, Analysis of in vitro demineralised human enamel using multi-scale correlative optical and scanning electron microscopy, and high-resolution synchrotron wide-angle X-ray scattering, Mater. Des. 206 (2021) 109739, http://dx.doi.org/10.1016/j.matdes.2021.109739.

[36] L.-L. Zhang, J.-Y. Li, X.-D. Zhou, F.-Z. Cui, L. Wei, Chemical and crystallographic study of remineralized surface on initial carious enamel treated with galla chinensis, Scanning 31 (6) (2009) 236–245, http://dx.doi.org/10.1002/sca.20176.

[37] A. Chaiwat, N. Thirasupa, O. Ajcharanukul, Use of micro-computed tomography and scanning electron microscopy with energy-dispersive spectroscopy to distinguish natural white spot enamel lesions from sound enamel in human premolars, Oral Sci. 66 (1) (2024) 50–54, http://dx.doi.org/10.2334/josnusd.23-0264.

[38] C. Wang, H. Xu, H. Tang, L. Xin, X. Huang, N. Wang, X. Zhao, X. Wei, R. Zhang, Fluorescence and reflectance-based dual-modal hyperspectral image fusion for caries diagnosis, Measurement 246 (2025) 116701, http://dx.doi.org/10.1016/j.measurement.2025.116701.

[39] S.E. Bishara, A.W. Ostby, J. Laffoon, J.J. Warren, Enamel cracks and ceramic bracket failure during debonding *in vitro*, Angle. Orthod. 78 (6) (2008) 1078–1083, http://dx.doi.org/10.2319/112007-540.1.

[40] A. Micheau, Occlusal fissure, 2023, https://www.imaios.com/en/e-anatomy/anatomical-structures/occlusal-fissure-121125208.

[41] M. Ryu, R. Honda, A. Balčytis, J. Vongsvivut, M.J. Tobin, S. Juodkazis, J. Morikawa, Hyperspectral mapping of anisotropy, Nanoscale Horiz. 4 (2019) 1443–1449, http://dx.doi.org/10.1039/C9NH00340A.

[42] R. Meguya, S.H. Ng, M. Han, V. Anand, T. Katkus, J. Vongsvivut, D. Appadoo, Y. Nishijima, S. Juodkazis, J. Morikawa, Polariscopy with optical near-fields, Nanoscale Horiz. 7 (2022) 1047–1053, http://dx.doi.org/10.1039/D2NH00187J.

[43] R. Honda, M. Ryu, M. Moritake, A. Balčytis, V. Mizeikis, J. Vongsvivut, M.J. Tobin, D. Appadoo, J.-L. Li, S.H. Ng, S. Juodkazis, J. Morikawa, Infrared polariscopy imaging of linear polymeric patterns with a focal plane array, Nanomater. 9 (5) (2019) 732, http://dx.doi.org/10.3390/nano9050732.

[44] X. Li, J. Wang, A. Joiner, J. Chang, The remineralisation of enamel: a review of the literature, J. Dent. 42 (2014) S12–S20, http://dx.doi.org/10.1016/S0300-5712(14)50003-6.

[45] D. Ricucci, J.F. Siqueira, Jr., S. Loghin, L.H. Berman, The cracked tooth: histopathologic and histobacteriologic aspects, J. Endod. 41 (3) (2015) 343–352, http://dx.doi.org/10.1016/j.joen.2014.09.021.

[46] A. Kishen, A. Shrestha, A. Rafique, Fiber optic backscatter spectroscopic sensor to monitor enamel demineralization and remineralization in vitro, J. Conserv. Dent.: JCD 11 (2008) 63–70, https://pmc.ncbi.nlm.nih.gov/articles/PMC2813093/.

[47] M. Ryu, H.-H. Huang, J. Vongsvivut, S.H. Ng, I. Dumbryte, D. Narbutis, M. Malinauskas, S. Juodkazis, J. Morikawa, Anisotropy analysis of bamboo and tooth using 4-angle polarization micro-spectroscopy, Nano Sel. 7 (3) (2026) e70099, http://dx.doi.org/10.1002/nano.70099.

[48] P.-Y. Collart-Dutilleul, S. Piglionico, R. Younes, Y. Messat, S. Garrabé, H. Salehi, J.-C. Durand, F. Cuisinier, A. Desoutter, Raman confocal microscopy atlas of human tooth, Arch. Oral. Biol. 173 (2025) 106189, http://dx.doi.org/10.1016/j.archoralbio.2025.106189.